Grain orientation dependent Nb–Ti microalloying mediated surface segregation on ferritic stainless steel

Harri Ali-Löytty[a], Markku Hannula[a], Mari Honkanen[b], Kauko Östman[b], Kimmo Lahtonen[a], and Mika Valden[a,*]

[a]Surface Science Laboratory, Optoelectronics Research Centre, Tampere University of Technology, P.O.B. 692, FI-33101 Tampere, Finland

[b]Department of Materials Science, Tampere University of Technology, P.O.B. 589, FI-33101 Tampere, Finland

Abstract

Surface segregation and oxide formation anisotropy on Ti–Nb stabilized ferritic stainless steel (EN 1.4521) were studied by XPS and Electron Backscatter Diffraction. Competitive surface segregation of Si, Nb and Ti was initiated at ~550 °C, and segregation was favored to the open surface sites of <111> oriented grains. Furthermore, the surface segregation of Cr was strongly limited at the locations of stable Ti(CN)- and (NbTi)C-type precipitates. Consequently, the oxidation resistance of stainless steels can be enhanced cost-efficiently, without alloy additions, by optimizing the microstructure to facilitate the fast and uniform growth of protective oxide scale.

Keywords: A. Stainless steel; B. XPS; B. SEM; C. Interfaces; C. Segregation; C. Oxidation

*To whom correspondence should be addressed. Tel.: +358 40 849 0261. E-mail address: mika.valden@tut.fi (M. Valden).

1. Introduction

Ferritic stainless steels (Fe–Cr alloys) with medium Cr (17–20 at.%), Mo, Ti and Nb alloying have been developed for high-temperature applications. These cost-efficient alloys provide good mechanical strength and corrosion resistance, and are therefore an excellent alternative to austenitic stainless steel grades (Fe–Cr–Ni alloys) in energy conversion and exhaust systems, where operation performance must be maintained at temperatures as high as 800 °C [1]. Recently, these alloys have attracted interest as interconnect materials for solid oxide fuel cells (SOFCs) operating at 600–800 °C [2]. However, because of the strict performance requirements for high electrical conductivity and low Cr evaporation, special ferritic stainless steel grades have been developed for SOFC interconnects with a particular emphasis on oxidation properties [3].

The Ti and Nb additions improve the mechanical properties by solution hardening while improving corrosion resistance by forming more stable compounds with residual C and N than Cr. The Mo alloying increases the stress corrosion resistance of steel. As a result of the relatively high degree of alloying, the microstructure is more susceptible to the precipitation of secondary phases such as carbonitrides and intermetallic Laves phases (e.g., Fe_2Nb) [4]. Laves phases have been shown to improve the high-temperature strength and creep resistance, and can also incorporate other alloying elements such as Cr, Mo, and Si. Recently, Juuti et al. showed that a $(FeCrSi)_2(MoNb)$-type Laves phase containing 6–10 at.% of Si forms on EN 1.4521 grade ferritic stainless steel upon a prolonged heat treatment at 650 °C [5], which can be utilized to improve electrical properties in SOFC interconnect

applications [4]. Conversely, Bitondo et al. have studied the influence of commercially available short annealing treatment (60 s at 1000 °C) on the corrosion behavior of the same steel grade and found little change in the microstructure accompanied with no change in corrosion resistance [6].

The corrosion resistance of stainless steels stems from the formation of a Cr rich protective oxide layer, which can be further improved for high-temperature applications by alloying with elements, such as Si, Al, Ti, Zr, Ce, Y, that form stable oxides at the oxide–metal interface [7]. These compounds contribute to the formation and adhesion of an oxide layer by acting as a diffusion barrier for scale forming elements (e.g. Cr, Mn, Fe). Huttunen-Saarivirta et al. studied corrosion performance of ferritic stainless steels under simulated exhaust gas condensate conditions and found Ti, Si and Nb additions crucial to the oxide scale properties [1]. Furthermore, the secondary phases can affect the oxidation properties either by incorporating scale forming elements, by blocking fast diffusion paths such as grain boundaries, or by impairing the adhesion of an oxide layer.

The oxidation properties of a stainless steel under specific conditions are largely determined by the elemental composition of the alloy, however, the microstructure and surface finish can also have an effect. The grain size of an alloy can be affected by heat treatment, whereas the texture, i.e., the grain orientation distribution, can be modified by hot and cold working. Grabke and co-workers have shown that small grain size and surface-working increase the corrosion resistance of steels under metal dusting conditions compared to large grain size and pickled or electropolished surface finish. The

improvement was attributed to the enhanced diffusion of Cr, Mn and Si through dislocations and grain boundaries [8]. Studies on nanocrystalline Fe–Cr alloys have shown that their corrosion resistance under aqueous conditions compared to coarse grained alloys can be either increased or decreased depending on the electrolyte [9]. At high temperatures, on the other hand, nanocrystalline alloys have been reported to exhibit higher oxidation resistance than microcrystalline alloys due to their higher degree of structural defects to act as fast diffusion channels for Cr [10].

The anisotropic nature of corrosion has been studied on austenitic stainless steel AISI 316L revealing that the high atomic density surface planes have higher resistance to pitting corrosion [11,12]. Meanwhile, segregation studies on Fe single crystal surfaces have shown favorable segregation of minor alloying elements to the low atomic density surface planes [13]. In general, the influence of the alloy's microstructure on corrosion properties has gained little attention compared to the influence on mechanical properties, despite the fact that through optimization of the microstructure, alloying additions could be reduced to achieve similar oxidation resistance [14].

In order to provide new insights into the influence of minor alloying elements and alloy microstructure on high-temperature oxidation of stainless steels we utilized surface sensitive spectromicroscopy techniques and annealing under ultra-high vacuum (UHV) conditions to study surface segregation on industrial Ti–Nb stabilized ferritic stainless steel (EN 1.4521, Fe–19Cr–1Mo–1Si–0.2Nb–0.1Ti (at.%)). The use of synchrotron radiation mediated X-ray Photoelectron Spectroscopy (XPS) provided better elemental and chemical

sensitivity to distinguish different chemical compounds on the surface compared to XPS with focused Al Kα laboratory source. The Scanning Electron Microscopy (SEM) and Electron Backscatter Diffraction (EBSD) analysis allowed us to correlate the surface chemical composition with microstructure and grain orientation. The obtained results show surface segregation and oxide formation anisotropy and competitive segregation of Si, Nb, and Ti at high-temperatures. These elements form secondary phases in FeCr alloys and contribute to the high-temperature oxidation by forming oxide compounds at the oxide scale–alloy interface. The influence of oxygen induced surface segregation and formation of stable oxide compounds was studied at low pO_2 in the temperature of 450–800 °C and correlated with segregation results on the metallic surface. These results can be utilized to optimize Nb–Ti stabilization, heat treatments and surface finish of ferritic stainless steel alloys to facilitate the fast growth of protective oxide layer under high-temperature conditions.

2. Experimental

The investigated EN 1.4521 ferritic stainless steel was supplied by Outokumpu Stainless Oy (Tornio, Finland). The composition of the bulk alloy is: 77.6 at.% Fe, 18.6 at.% Cr, 1.2 at.% Mo, 1.0 at.% Si, 0.5 at.% Mn, 0.2 at.% Ni, 0.2 at.% Nb, 0.1 at.% Ti, 0.2 at.% Cu, 0.01 at.% Al and 0.06 at.% C. In addition, the alloy contains very low concentrations of other minor and residual elements such as N, P, and Sn. A disk-shaped sample (1 mm thick, diameter of 9 mm) was cut from a cold rolled, heat treated, pickled and skin passed sheet (i.e. 2B surface finish). The microstructure of the sample was characterised with a field

emission Scanning Electron Microscope (FESEM, Zeiss ULTRAplus) equipped with an Electron Backscatter Diffraction (EBSD) system and an Energy Dispersive X-ray Spectrometer (EDX, INCA Energy 350 analysator with INCAx-act silicon-drift detector).

Surface segregation experiments and XPS measurements were carried out in two separate surface analysis systems under controlled UHV atmosphere with base pressures below 1×10^{-8} Pa. After loading the samples into the system, atmospheric impurities and native oxides were first removed by cycles of 2.0 keV Ar^+ ion sputtering at 25 °C and subsequent annealing at 800 °C for 5 min. A surface segregation experiment to a metallic surface was carried out by annealing a sputter cleaned sample and simultaneously recording XPS spectra. The temperature was raised to the target value starting at 450 °C, where XPS spectra were recorded after 5 min holding time. After data acquisition the temperature was increased in 50 °C increments up to 800 °C. Total duration of the experiment was 90 min, during which the pressure remained below 1.0×10^{-7} Pa.

A surface segregation experiment on an oxidized surface was carried out by cumulative annealing of an oxidized surface at target temperatures of 450, 650, and 800 °C for 30 min. The chemical composition of the surface was subsequently analyzed by XPS and Energy Filtered Photoemission Electron Microscopy (EF-PEEM) at 25 °C. Prior to the experiment, the surface had been sputter cleaned, annealed at 450 °C for 5 min and oxidized by backfilling the chamber with 8.0×10^{-4} Pa of O_2 (99.9999 %) for 2500 s at 25 °C.

XPS and EF-PEEM measurements employing laboratory sources were carried out using a NanoESCA (Omicron NanoTechnology GmbH) spectromicroscopy system [15].

Monochromatized focused Al Kα radiation (hν = 1486.5 eV, ULVAC-PHI model 36-100 Focused X-ray source) was utilized for core level spectroscopy and imaging, whereas, a secondary electron tail cut-off map for work function determination was measured with non-monochromatized He Iα radiation (hν = 21.22 eV) using HIS 13 VUV source (Focus GmbH). Reported work function values were corrected for the Schottky effect of –0.098 eV induced by the 12 kV analyzer extractor voltage [16]. Total energy resolutions for core level spectroscopy and work function measurements were 0.48 and 0.05 eV, respectively, and lateral resolutions for core level and work function imaging were 0.5 and 0.1 μm, respectively. The core level images were recorded with 1.6 eV band pass energy.

The XPS measurements employing synchrotron radiation were performed at the soft X-ray beamline I311 in the synchrotron radiation facility MAX IV Laboratory (Sweden). The beamline and the experimental endstation have been described in Ref. [17]. In short, I311 is an undulator beamline with a modified SX-700 monochromator and an endstation equipped with a hemispherical SCIENTA SES-200 electron analyzer. The total energy resolutions were 0.15 (hν = 400 eV) and 0.23 eV (hν = 688 eV). The analysis area in both XPS setups was large in comparison to the average grain size of the sample; therefore the XPS spectra represent surface analysis over a large number of individual grains.

The chemical states of elements were determined from XPS spectra by least-squares fitting of asymmetric Gaussian–Lorentzian lineshapes to the photoelectron peaks after subtracting a Shirley background with the exception of the Nb 3d spectra measured with hν = 400 eV that was fitted by asymmetric Doniach–Sunjic lineshapes after a linear background

subtraction. The inelastic electron background subtraction from the core-level EF-PEEM images was done by subtracting a linear background defined by the intensity of two images measured at lower and higher binding energy side of the main peak. The data analysis was made by using CasaXPS software (version 2.3.16) [18] and Scofield photoionization cross-sections were used for the determination of relative atomic concentrations (hν = 1486.5 eV) [19]. The binding energy scale was calibrated either with the metallic Fe $2p_{3/2}$ peak set to 707.0 eV (hν = 1486.5 eV) or according to the Fermi edge (hν = 400, 688 eV).

It is worth mentioning that the inelastic mean free path of electrons (IMFP, λ) depends on the kinetic energy of the electrons. The kinetic energy of the photoelectrons, on the other hand, depends on the photon energy and photoelectron transitions (core levels) that are used for the analysis [20]. In general, the XPS information depth (3λ) for a given transition decreases with decreasing photon energy, e.g. in the case of Nb 3d from 5.9 nm (hν = 1486.6 eV) to 1.7 nm (hν = 400 eV), as determined by the TPP-2M equation for the Fe medium [21].

3. Results and discussion

3.1. Microstructure and work function anisotropy of EN 1.4521

SEM and EBSD micrographs in Figs. 1(a) and (b) show the surface of the as received sample, i.e., microstructure of the bulk sample, indicating the presence of different types of precipitated particles and grain orientations. In addition to highly stable Ti(CN)- and (NbTi)C-type precipitates some $(FeCrSi)_2(MoNb)$-type intermetallic Laves phase particles were present in the as received alloy on grain boundaries and in grain interiors originating

from the conventional industrial processing stages of the alloy. The lower left grain was particularly rich in small (< 1 μm in diameter) Laves particles as evidenced by the bright contrast in the SEM figure in (a) and the dark contrast in the band contrast (BC) map in (b). Precipitation phenomena on this alloy were studied by Juuti et al., and it was found that the Laves phase particles increase in number and size substantially within 120 h heat treatment at 650 °C and dissolve within 24 h at 1050 °C [5]. In order to avoid microstructural changes during the experiments excessive heat treatments were avoided in our study.

Figs. 1(c) and (d) show a work function map and relative Cr concentration (relative to the total amount of Cr and Fe) for the sample surface after sputter cleaning and annealing at 450 °C in UHV, and thus indicate the initial surface condition for the surface segregation experiments. The work function ranged from 4.32 to 4.57 eV and had an average value of 4.44 eV. The relative Cr concentration varied between 18.8 and 25.2 at.% for different grains. The relative average Cr concentration on the surface was 20.5 at.%, which was slightly above the relative bulk Cr concentration of 19.3 at.%.

Sputter cleaning by energetic Ar^+ ions does not only remove surface layers but can also induce chemical and structural changes to the sample surface [22]. In particular, different elements in alloys and compounds may have different sputtering rates that will cause enrichment of an element with lower sputtering yield. This preferential sputtering is affected primarily by mass effects and surface binding energy effects [23]. If surface binding energies are similar, enrichment of heavier component is expected. However, preferential sputtering in alloys is often difficult to predict from surface binding energies of

pure elements since those can be different in alloys [24]. At low temperatures, ion bombardment induced defects can enhance surface segregation but at higher temperatures the segregation results from the usual diffusion process [22].

Yacou et al. studied theoretically 3 keV Ne ion bombardment induced surface effects in Fe–Cr–Ni alloys at elevated temperatures [25]. They found that ion beam effects dominated the changes in the surface composition below 200 °C but thermally induced segregation became increasingly important for the final surface composition at higher temperatures. In the present study, the small difference between average Cr surface concentrations after sputtering and subsequent annealing at 450 °C in UHV and the Cr bulk concentrations allows us to conclude that sputtering effects play only little role to the surface composition in the case of primary alloying elements Fe and Cr, and that such a pretreatment provides us an excellent surface for our temperature induced segregation experiments.

In the case of minor alloying elements and secondary phase particles, it was not possible to exclusively address preferential sputtering effects due to low surface concentrations of these elements. The sputtering rate of metal carbides and nitrides is often different from metals. For example, Zalar et al. reported lower sputtering rate for Cr and Ti carbides compared to metals, while WC had higher sputtering rate than W [26,27]. Consequently, during prolonged sputtering treatments enrichment of precipitates with lower sputtering rate compared to alloy matrix is expected. Therefore, in order to mitigate preferential sputtering effects between the alloy matrix and secondary phase particles excessive sputtering was avoided in our study, and the sample was not sputter cleaned in the middle of segregation

series presented in Sections 3.2 and 3.3. The sputtered layer thickness during a cleaning cycle was approximated to be 10 nm using Ta_2O_5 reference, and the total sputtering depth during the experiment was smaller than the size of secondary phase particles of interest (< 1 µm). Even so, the sputter cleaning may have altered the number density of secondary phase precipitates on the sample surface compared to the bulk alloy. It should be noted, though, that the amount of different secondary phase particles depends on the exact alloy composition that is different even within the same steel grade, and thus, the sputter cleaned and annealed surface of ours should be considered merely a representative model system and only qualitative comparison with the literature is reasonable [5].

The work function is a surface property that is sensitive to both the chemical composition and the structure of the surface. The measured values are lower than the literature values for Fe (4.67–4.81 eV) but agree with Cr (4.5 eV) [28]. However, the work function histogram shows dominance at lower energies between 4.35 and 4.45 eV, which suggests the presence of other elements on the surface. In particular, Nb (3.95–4.87 eV) and Ti (4.33 eV) termination agrees with the measurement [28]. In contrast, oxygen termination of a transition metal surface has tendency to increase the work function, which can therefore be excluded [29]. On the other hand, the lowest work function on the body-centered cubic (bcc) EN 1.4521 sample was measured for <111> crystal orientation with low surface atom density with the values increasing towards <100> and <101> crystallographic directions, which indicates work function anisotropy. The increase in the work function with increasing surface atom density agrees qualitatively with similar experiments on copper and austenitic 316L stainless steel that have face-centered cubic structures [16,30].

No correlation between work function and relative Cr concentration was found. The biggest Cr concentration (25.2 at.%) was measured for the lower left grain in Fig. 1 with high number density of Laves particles. We conclude that the enrichment of Nb and Mo in the Laves particles replaces Fe, which increases the relative Cr concentration on grains with high number density of Laves particles.

3.2. Segregation to a metallic surface

Surface segregation experiment to metallic surface was carried out by annealing a sputter cleaned sample in UHV and simultaneously recording XPS spectra. Fig. 2 shows the normalized XPS signal intensities for Si 2p, Nb 3d, Ti 2p, Fe 3p, Cr 3p, and Mo 3d.

Only little change in the surface chemical composition was observed until the sample reached 500 °C, above which the surface enrichment of microalloying and trace elements took place at the expense of primary alloying elements Fe, Cr and Mo. The highest surface concentration of Si, Nb and Ti was measured at distinct temperatures of 600, 650, and 700 °C, respectively. At high temperatures, XPS signals of the following minor alloying and trace elements were also detected (the temperature at which the maximum surface concentration was reached is depicted in parenthesis): Cu (650 °C); As, P (700 °C); N (750 °C); Sb, Sn, Al (800 °C). Besides Al, these elements were not detected on the surface upon surface segregation experiment to an oxidized surface. Al alloying enhances high-temperature corrosion resistance of Fe alloys upon formation of α-Al_2O_3 at temperatures above 900 °C that were beyond the scope of this article [31]. In addition, residual amounts of oxygen and carbon were detected on the surface at all temperatures, but the majority of

carbon was dissolved into the bulk as temperature exceeded 500 °C (not shown). In contrast to the results on oxygen induced segregation in Section 3.3., Mn was not detected on the surface during the experiment on the metallic surface.

Fig. 3 depicts the evolution of Si 2p, Nb 3d and Ti 2p XP spectra as a function of temperature. The different chemical states of Si, Nb and Ti surface species can be validated by the chemical shifts in the XPS transitions. The Si 2p transition was fitted using two doublets (doublet separation of 0.608 eV and area branching ratio of 0.50) corresponding to the $2p_{3/2}$ and $2p_{1/2}$ levels of Si. Adequate fitting of the complex structure of the Nb 3d spectra required four duplets (doublet separation of 2.78 eV and area branching ratio of 0.67) corresponding to the $3d_{5/2}$ and $3d_{3/2}$ levels of Nb. Ti 2p was fitted using two components fitted to the Ti $2p_{3/2}$ peak that was clearly separated from the $2p_{1/2}$ peak.

Up to the temperature of 600 °C the Si 2p transition showed only one component with Si $2p_{3/2}$ at 98.5 eV, whereas at higher temperatures a second component at 98.9 eV appeared. The first component is assigned to elemental Si^0, and the second component to the formation of metal silicides (M_xSi), most likely Nb silicides, on the surface [32]. It is worth noting that the formation of oxidized Si on the surface was to a large extent avoided as evidenced by low intensity at 103 eV corresponding to Si^{4+} (SiO_2). This is due to the low amount of residual oxygen in the alloy to segregate to the surface, and also the purity of the UHV conditions during the experiments.

The Nb 3d spectra in Fig. 3(b) shows four $3d_{5/2}$ components at 202.9 eV (Nb^0), 203.5 eV (Nb_x), 203.8 eV (Nb^+) and 204.2 eV (Nb^{2+}) corresponding to elemental Nb and different

oxidation states in accordance with Ref. [32]. The binding energy of Nb_x peak corresponds to NbC and a non-stoichiometric Nb oxide (e.g. Nb_xO, $x > 2$), and therefore, Nb_x peak cannot be reliably assigned to a single chemical compound. Up to temperatures of 600 °C, Nb was found to segregate with oxygen, but at 650 °C, an elemental Nb^0 peak appears and increases in intensity at 700 °C at the expense of oxidized Nb. The binding energy of elemental Nb^0 in Fe–Cr solutions is also in agreement with Nb silicide ($NbSi_2$ 202.9 eV [33]) in accordance with the Si 2p spectra in Fig. 3(a).

Apart from the spectrum recorded at 700 °C, the Ti 2p transition in Fig. 3(c) shows only one component with $2p_{3/2}$ peak at 454.8 eV (Ti^{2+}) corresponding to oxidized Ti. At 700 °C, however, a second component appears at 453.9 eV (Ti^0). Based on the evolution of the Si, Nb and Ti XP spectra, it is apparent that there is strong competition for the trace amount of oxygen on the surface. Surface oxygen is bound to the most stable compounds available, which is determined by the segregation kinetics of elements. Si, Nb and Ti form more stable oxides than Fe and Cr, and therefore, these elements are critical to the high temperature oxidation resistance of stainless steel alloys.

The driving force for surface segregation is the minimization of surface energy, but segregation kinetics is strongly affected by the diffusivities and concentrations of segregants. As a result, most elements which can be dissolved in steel tend to enrich to surface at high temperatures [7,13]. Likewise, the enrichment of Al, Sn and Sb at 800 °C is in accordance with their low surface energies 1.143, 0.675 and 0.535 J/m^2, respectively, compared to Cr (2.300 J/m^2) and Fe (2.417 J/m^2) [34]. In contrast, based on surface

energies of pure elements, segregation of Nb (2.655 J/m^2) on Fe–Cr alloy surface would not be expected. Distinct temperatures at which Si, Nb and Ti reach the maximum surface concentration suggest competition for the same surface sites. Interestingly, Cr enrichment to the surface was not observed, which can be attributed to the high degree of alloying, and especially, to the sufficient Ti stabilization and formation of TiN precipitates. Without Ti stabilization, strong cosegregation of Cr with residual N can occur in ferritic stainless steel alloys at temperatures above 500 °C [35].

Bearing in mind that the alloy is susceptible to the formation of $(FeCrSi)_2(MoNb)$-type intermetallic Laves phase, it is particularly interesting that the surface segregation of Si precedes segregation of Nb. Incorporation of Si to the $(FeCr)_2Nb$ -type Laves phase particles has been recently utilized to enhance the electrical properties of ferritic stainless steels in a solid oxide fuel cell (SOFC) interconnect application that operate typically at 650 °C [32,36]. The observed temperature dependence of Si and Nb surface segregation suggests that chemical composition of Laves phase particles, in terms of Si concentration, could be optimized by heat treatment at temperatures below the typical SOFC operation temperature. This suggestion is supported by the work of Kato et al. in Ref. [37] where $(Fe, Cr)_2Nb$ -type Laves particles with higher Si content were measured after heat treatment at 800 °C vs. 900 °C on high purity 17Cr–0.5Nb steel. On the other hand, local enrichment of P has been shown to facilitate the nucleation of Laves particles next to carbides at grain boundaries [38]. Strong surface segregation of P was observed at 700 °C suggesting that the precipitation of Laves particles at the grain boundaries versus at grain interiors could be temperature dependent. In contrast, the peak intensity for Mo had already been detected at

500 °C suggesting that Mo enrichment to the Laves particles is not mediated by temperature. Moreover, segregation of Mo to the grain boundaries of martensitic-ferritic steel (Fe–12Cr–1 Mo, wt.%) was shown to precede the nucleation of Laves phase at 550 °C [39].

3.3. Segregation to an oxidized surface

In order to study the role of surface oxygen in the segregation of microalloying elements in more detail, a surface segregation experiment was performed by oxidizing the surface before annealing. The oxygen exposure in 8.0×10^{-4} Pa O_2 for 2500 s at 25 °C simulates the formation of 2–3 nm thick native oxide layer on stainless steel alloy [40]. Before oxygen exposure, the surface was sputtered and subsequently annealed at 450 °C, which was found to be an insufficient temperature for promoting segregation of Si, Nb and Ti to the surface as shown above. After oxidation the surface was post-annealed in UHV at the target temperature for 30 min before XPS and EF-PEEM measurements that were conducted at 25 °C. Post-annealing in UHV drives the surface towards thermodynamic equilibrium by overcoming the kinetic restraints resulting in the formation of the most stable chemical compounds on the surface [41]. For comparison to the high-temperature oxidation experiments under ambient air conditions these compounds form at the oxide scale–metal interface where the oxygen activity is low, i.e., low pO_2.

Fig. 4 shows a series of XP spectra measured from the sputter cleaned sample followed by subsequent annealing at 450 °C (unoxidized), after oxygen exposure in 8.0×10^{-4} Pa O_2 for 2500 s at 25 °C, and after 30 min annealing at 450–800 °C. The spectra in Fig. 4 show the

spatially averaged information on the sample surface, whereas the EF-PEEM images in Figs. 5 and 6 depict the local chemical information. The contrast in the compositionally sensitive EF-PEEM images is determined by the band pass energy window (1.6 eV), which is indicated by green lines in Fig. 4.

The unoxidized surface consisted of mainly Fe^0 (Fe $2p_{3/2}$ at 707.0 eV), Cr^0 (Cr $2p_{3/2}$ at 574.7 eV) and Mo^0 (Mo $3d_{5/2}$ at 227.7 eV) primarily in their metallic form. The trace amount of oxygen (< 5 at.%) visible in the O 1s spectrum in Fig. 4(h) was mainly bound to Cr as indicated by a shoulder at 576.5 eV in the Cr $2p_{3/2}$ peak in 4(b). In addition, the O 1s image in Fig. 5 reveals a higher amount of metal oxides (530.9 eV) at the Ti(CN) and (NbTi)C precipitate locations, suggesting the presence of oxidized Ti and Nb that can barely be resolved from the spectra in Figs. 4(f) and 4(g). Interestingly, the distribution of metallic Fe in Fig. 5 was inhomogeneous following the grain structure of the sample, whereas, metallic Cr was more homogeneously distributed on the surface.

After 15 kL oxidation at 25 °C, an oxide layer of Cr^{3+} (Cr $2p_{3/2}$ at 576.5 eV), $Fe^{2+/3+}$ (Fe $2p_{3/2}$ at 710.2 eV) and Mo^{4+} (Mo $3d_{5/2}$ at 228.9 eV) formed on the surface (Fig. 4). The thickness of the oxide layer was only few nanometers as evidenced by XPS signals of metallic Fe, Cr, and Mo that were clearly resolved after oxidation. The increased intensity of Cr^{3+} peak indicates that the oxide layer was enriched with Cr at the expense of Fe and Mo in accordance with the typical composition of native oxide layer on stainless steel (Fe–Cr) alloys [42]. In contrast to the inhomogeneous distribution of metallic Fe before oxidation, both Fe and Cr oxide distributions were homogeneous after oxidation (Fig. 5).

After annealing at 450 °C in UHV, strong surface enrichment and oxidation of Cr were observed, while the majority of Fe oxides were reduced. Conversion of mixed Fe–Cr–Mo oxide to primarily Cr oxide induced a shift in the O 1s peak position from 530.4 to 531.2 eV. The presence of Cr rich surface oxide is also supported by similar intensity distribution of Cr 2p (576.8 eV, Cr^{3+}) and O 1s images in Fig. 5. It is worth noting that XPS signals of Nb 3d and Ti 2p are barely resolved from the spectra in Fig. 5, whereas corresponding images in Fig. 6 show that Nb and Ti are enriched at the Ti(CN) and (NbTi)C precipitate locations. In contrast, $(FeCrSi)_2(MoNb)$-type Laves particles were not resolved from the Nb and Si images most likely due to their small size (< 1 µm in diameter) compared to the spatial resolution of core level EF-PEEM images (0.5 µm). Interestingly, the surface segregation of Cr is strongly limited at the Ti(CN) and (NbTi)C precipitate locations which has implications for the growth of protective Cr rich oxide scale under high-temperature conditions. Slow diffusion of Cr at the precipitate locations can reduce oxidation resistance and increase susceptibility to localized corrosion [43]. After annealing at 650 °C, strong surface segregation and oxidation of Mn (Mn $2p_{3/2}$ at 641.7 eV, Mn^{2+}), Si (Si 2p at 103.0 eV, Si^{4+}) and Nb (Nb $3d_{5/2}$ at 204.2 eV, Nb^{2+}) took place while Fe and Mo oxides were completely reduced and oxidized Cr partly reduced to metallic state. Fig. 5 reveals a similar spatial distribution for oxidized Mn and Cr supporting formation of $(Mn, Cr)_3O_4$ spinel oxide [44]. The Si 2p image in Fig. 6 shows higher intensity on the <111> oriented grain that suggests grain orientation dependent surface segregation.

Surprisingly, after annealing at 800 °C, the Mn 2p XPS signal completely disappeared (Fig. 4 (d)) which serves as an evidence of lower stability of $(Mn, Cr)_3O_4$ spinel oxide compared

to Si and Ti oxides and diffusion of Mn to the bulk phase. The formation of $(Mn, Cr)_3O_4$ surface oxide is particularly important in SOFC interconnect application where Mn rich surface oxide mitigates the evaporation of volatile Cr species under moist operation conditions. On the other hand, the Mn to Cr ratio of $(Mn, Cr)_3O_4$ spinel oxide can be affected by heat treatment as demonstrated in the case of $(FeCrSi)_2$(Nb)-type Laves forming EN 1.4509 (Fe–19Cr–0.9Si–0.2Nb, at.%) alloy [32]. The influence of precipitation on oxide scale formation at 650 °C on EN 1.4521 will be studied in our forthcoming article.

Furthermore, at 800 °C strong surface segregation and oxidation of Ti (Ti $2p_{3/2}$ at 458.6 eV, Ti^{4+}) took place in addition to the reduction of Cr and Nb oxides. Interestingly, the Si^{4+} (SiO_2) XPS peak prevails, while a significant peak of metallic Ti^0 appears together with oxidized Ti^{4+} (TiO_2). By comparing the standard free energies of formation of SiO_2 (–674 kJ mol^{-1} of O_2) and TiO_2 (–704 kJ mol^{-1} of O_2) at 800 °C [28], complete oxidation of Ti at the expense of SiO_2 reduction was expected. Hence, it can be concluded that the reaction was kinetically hindered given that the metal–oxide bond energies between Ti–O and Si–O are similar, whereas reduction of less stable NbO (–558 kJ mol^{-1} of O_2) and Cr_2O_3 (–528 kJ mol^{-1} of O_2) was congruent with the thermodynamic data.

At 800 °C, Fig. 6 shows higher Ti 2p and Nb 3d intensity for the same <111> oriented grain that was enriched with Si at 650 °C. This confirms the grain orientation dependence of segregation, and in particular that surface segregation of microalloying elements Si, Nb, and Ti is favored on <111> oriented grains. The <111> orientation of bcc structure has low surface atom density that provides an open surface with enough space to reach high

occupancy of segregants. This result is in accordance with segregation studies on bcc Fe single crystal surfaces, where formation of dense p(1×1) structure of several segregants was reported to form on the <111> surface and sparse c(2×2) structure formed on the <100> surface with high surface atom density [13]. Furthermore, from the intensity distribution of Nb and Ti images it can be concluded that Ti(CN)- and (NbTi)C-type precipitates neither dissolved nor coarsened during the annealing experiments between 450–800 °C. The grain structure was not affected by the treatments.

No contrast difference in the EF-PEEM images was observed between grain boundaries and grain interiors. Grain boundaries of alloys can act as fast diffusion paths for elements affecting precipitation and oxide scale formation at high temperatures. Horita et al. observed preferential oxide formation on top of grain boundaries and enrichment of Mn at the grain boundaries of Fe–Cr alloy (ZMG232L) after 144 h oxidation at 800 °C using secondary ion mass spectroscopy (SIMS) depth profiling [45]. The apparent discrepancy between the observations can be explained by the different experimental conditions and analysis methods. Our experiments were conducted in UHV without O_2 that prevented the oxide layer growth during annealing. In terms of surface sensitivity, both EF-PEEM and SIMS have information depth of few nm compared to few µm information depth of EDX analysis. With that in mind, in Ref. [45] using SIMS analysis, Mn enrichment at the grain boundaries was not observed at the surface of oxidized Fe–Cr alloy , but it was observed at the oxide–alloy interface (Fig. 7 in Ref. [45]), which is in line with our results.

The grain orientation dependent surface segregation of Si, Nb, and Ti has direct consequences on the formation of protective oxide layer at high-temperatures. The formation of Si, Nb, and Ti oxides at the oxide–alloy interface controls the growth rate of Cr rich outer oxide scale by acting as a diffusion barrier. The segregation anisotropy explains the anisotropy of oxidation rate that is often observed on stainless steel alloys [1]. Phaniraj et al. studied oxidation of ferritic stainless steel (Crofer22APU, Fe–23Cr–0.02Si–0.07Ti, wt.%) at 650 °C in air, and found that after 1 h oxidation the <111> oriented grains were oxidized more rapidly than the other grains, which confirms the observed orientation dependence of surface segregation [46]. Inhomogeneous oxide layer growth rate can lead to the evolution of stress within the scale that finally causes spallation. Such phenomenon is most likely under high oxidation rate conditions and on alloys with strong texture. On the other hand, the oxide layer growth rate at high-temperatures could be decreased by optimizing the texture to mediate the fast diffusion of Si, Nb and Ti to the surface, that would in return, allow the use of lower alloying additions to obtain the same oxidation resistance [14].

Recently, metallic nanoparticles within an oxide scale on an Fe–Cr alloy were detected [47]. These nanoparticles are able to form a network through the oxide scale to serve as a diffusion channel for carbon and hydrogen without the need for oxide defects required in previous diffusion models. Diffusion of carbon and hydrogen through an oxide scale can be highly deterious causing brittleness and localized corrosion. On the other hand, metallic channels through an oxide scale can be beneficial increasing the electrical conductivity of metallic interconnects for SOFCs. The formation of such diffusion channels requires the

alloy to go through an oxide scale growth process during which an alloying element first forms an oxide that at later stages reduces to metal within the oxide scale of more stable oxide compounds, i.e. at low pO_2. Our results provide insights to such processes suggesting that Ti–Nb microalloying of ferritic stainless steel mediates segregation of metallic Ti and Nb to the surface at 800 °C when pO_2 is low, while oxygen is bound to highly stable oxide compounds of, e.g. Si and Al. By optimizing the alloy composition and microstructure via heat treatments, it may be possible to control the formation of Ti/Nb metallic nanoparticles on ferritic stainless steels during cyclic high-temperature oxidation processes.

4. Conclusions

Grain orientation dependence on surface segregation and formation of stable oxide compounds at low pO_2 were studied on Ti–Nb stabilized ferritic stainless steel (EN 1.4521, Fe–19Cr–1Mo–1Si–0.2Nb–0.1Ti (at.%)) between 450–800 °C in UHV by XPS, Energy Filtered Photoemission Electron Microscopy (EF-PEEM) and Electron Backscatter Diffraction (EBSD). On a metallic surface, competitive surface segregation of minor alloying elements was driven by temperature, and maximum surface concentrations of Si, Nb, and Ti were obtained at 600, 650, and 700 °C, respectively. During annealing of an oxidized sample, the surface oxide underwent a temperature induced transformation of Cr/Fe oxides (25 °C) to more stable Cr oxide at 450 °C, Si/Nb/Mn oxides at 650 °C, and Ti/Si oxides at 800 °C. Grain orientation showed only little influence on the formation of a Cr oxide rich passive layer at 25 °C. At high-temperatures, segregation of Si, Nb and Ti was favored to the open sites of <111> oriented grains that had the lowest work function.

Segregation and oxidation of minor alloying elements (Si, Nb, Ti) are crucial to the high-temperature performance of stainless steels, by affecting the microstructure via precipitation of secondary phases and through the formation of protective oxide scale. The EN 1.4521 alloy is susceptible to the formation of $(FeCrSi)_2(MoNb)$-type Laves phase at 450–800 °C, which was largely avoided by minimizing the exposure to high-temperatures. Ti(CN)- and (NbTi)C-type precipitates originating from the industrial processing of the alloy neither dissolved nor coarsened during the experiments but the surface segregation of Cr was strongly limited at the precipitate locations. The oxidation resistance of a stainless

steel alloy can be increased, without alloy additions, by facilitating the fast growth of protective oxide layer that can be achieved by optimizing the texture and precipitate structure.

Acknowledgments

The authors wish to acknowledge Mrs. Mirva Kujansuu and Mr. Jukka Säynäjäkangas (Outokumpu Stainless Oy) for providing the investigated stainless steel material and Mr. Timo Juuti for the discussion on the precipitation properties of the alloy (University of Oulu, Finland). We are grateful to the staff of MAX IV Laboratory for the assistance during the measurements. We gratefully acknowledge the financial support from the Academy of Finland (grant Nos. 141481 and 286713).

References

[1] E. Huttunen-Saarivirta, V.-T. Kuokkala, P. Pohjanne, Thermally grown oxide films and corrosion performance of ferritic stainless steels under simulated exhaust gas condensate conditions, Corros. Sci. 87 (2014) 344–365.

[2] N. Mahato, A. Banerjee, A. Gupta, S. Omar, K. Balani, Progress in material selection for solid oxide fuel cell technology: A review, Prog. Mater. Sci. 72 (2015) 141–337.

[3] N. Shaigan, W. Qu, D.G. Ivey, W. Chen, A review of recent progress in coatings, surface modifications and alloy developments for solid oxide fuel cell ferritic stainless steel interconnects, J. Power Sources 195 (2010) 1529–1542.

[4] K.H. Lo, C.H. Shek, J.K.L. Lai, Recent developments in stainless steels, Mater. Sci. Eng. R 65 (2009) 39–104.

[5] T. Juuti, L. Rovatti, A. Mäkelä, L.P. Karjalainen, D. Porter, Influence of long heat treatments on the laves phase nucleation in a type 444 ferritic stainless steel, J. Alloys Compd. 616 (2014) 250–256.

[6] C. Bitondo, A. Bossio, T. Monetta, M. Curioni, F. Bellucci, The effect of annealing on the corrosion behaviour of 444 stainless steel for drinking water applications, Corros. Sci. 87 (2014) 6–10.

[7] H.J. Grabke, Segregation and oxidation, Mater. Tehnol. 40 (2006) 39–47.

[8] C. Ostwald, H.J. Grabke, Initial oxidation and chromium diffusion. I. Effects of surface working on 9–20% Cr steels, Corros. Sci. 46 (2004) 1113–1127.

[9] R.K. Gupta, N. Birbilis, The influence of nanocrystalline structure and processing route on corrosion of stainless steel: A review, Corros. Sci. 92 (2015) 1–15.

[10] R.K.S. Raman, R.K. Gupta, Oxidation resistance of nanocrystalline vis-à-vis microcrystalline Fe–Cr alloys, Corros. Sci. 51 (2009) 316–321.

[11] A. Shahryari, J.A. Szpunar, S. Omanovic, The influence of crystallographic orientation distribution on 316LVM stainless steel pitting behavior, Corros. Sci. 51 (2009) 677–682.

[12] D. Lindell, R. Pettersson, Crystallographic effects in corrosion of austenitic stainless steel 316L, Mater. Corros. 66 (2015) 727–732.

[13] H.J. Grabke, V. Leroy, H. Viefhaus, Segregation on the Surface of Steels in Heat Treatment and Oxidation, ISIJ Int. 35 (1995) 95–113.

[14] B.V. Mahesh, R.K.S. Raman, Role of Nanostructure in Electrochemical Corrosion and High Temperature Oxidation: A Review, Metall. Mater. Trans. A 45 (2014) 5799–5822.

[15] O. Renault, M. Lavayssière, A. Bailly, D. Mariolle, N. Barrett, Core level photoelectron spectromicroscopy with Al Kα1 excitation at 500 nm spatial resolution, J. Electron Spectrosc. Relat. Phenom. 171 (2009) 68–71.

[16] O. Renault, R. Brochier, A. Roule, P.-H. Haumesser, B. Krömker, D. Funnemann, Work-function imaging of oriented copper grains by photoemission, Surf. Interface Anal. 38 (2006) 375–377.

[17] R. Nyholm, J.N. Andersen, U. Johansson, B.N. Jensen, I. Lindau, Beamline I311 at MAX-LAB: a VUV/soft X-ray undulator beamline for high resolution electron spectroscopy, Nucl. Instrum. Methods Phys. Res. Sect. Accel. Spectrometers Detect. Assoc. Equip. 467-468 (2001) 520–524.

[18] N. Fairley, CasaXPS: Spectrum Processing Software for XPS, AES and SIMS, 2011. http://www.casaxps.com/.

[19] J.H. Scofield, Hartree-Slater subshell photoionization cross-sections at 1254 and 1487 eV, J. Electron Spectrosc. Relat. Phenom. 8 (1976) 129–137.

[20] D. Briggs, XPS: Basic Principles, Spectral Features and Qualitative Analysis, in: D. Briggs, J.T. Grant (Eds.), IM Publications, Trowbridge, 2003: pp. 31–56.

[21] S. Tanuma, C.J. Powell, D.R. Penn, Calculations of electron inelastic mean free paths. V. Data for 14 organic compounds over the 50–2000 eV range, Surf. Interface Anal. 21 (1994) 165–176.

[22] A.W. Czanderna, T.E. Madey, C.J. Powell, Beam Effects, Surface Topography, and Depth Profiling in Surface Analysis, Kluwer Academic Publishers, Hingham, US, 1998.

[23] V.S. Smentkowski, Trends in sputtering, Prog. Surf. Sci. 64 (2000) 1–58.

[24] G. Betz, Alloy sputtering, Surf. Sci. 92 (1980) 283–309.

[25] A.M. Yacout, N.Q. Lam, J.F. Stubbins, Near-surface compositional modifications of ternary alloys during sputtering at elevated temperatures, Nucl. Instrum. Methods Phys. Res. Sect. B Beam Interact. Mater. At. 42 (1989) 49–60.

[26] A. Zalar, J. Kovač, B. Praček, P. Panjan, M. Čeh, Ion sputtering rates of W-, Ti- and Cr-carbides studied at different Ar+ ion incidence angles, Appl. Surf. Sci. 254 (2008) 6611–6618.

[27] A. Zalar, J. Kovač, B. Praček, P. Panjan, M. Čeh, Ion sputtering rates of C, CrxCy, and Cr at different Ar+ ion incidence angles, Vacuum. 82 (2007) 116–120.

[28] W.M. Haynes, D.R. Lide, CRC Handbook of Chemistry and Physics, 92nd ed., CRC Press, 2011.

[29] M.T. Greiner, L. Chai, M.G. Helander, W.-M. Tang, Z.-H. Lu, Transition Metal Oxide Work Functions: The Influence of Cation Oxidation State and Oxygen Vacancies, Adv. Funct. Mater. 22 (2012) 4557–4568.

[30] N. Barrett, O. Renault, H. Lemaître, P. Bonnaillie, F. Barcelo, F. Miserque, M. Wang, C. Corbel, Microscopic work function anisotropy and surface chemistry of 316L stainless steel using photoelectron emission microscopy, J. Electron Spectrosc. Relat. Phenom. 195 (2014) 117–124.

[31] E. Airiskallio, E. Nurmi, M.H. Heinonen, I.J. Väyrynen, K. Kokko, M. Ropo, M.P.J. Punkkinen, H. Pitkänen, M. Alatalo, J. Kollár, B. Johansson, L. Vitos, High temperature oxidation of Fe–Al and Fe–Cr–Al alloys: The role of Cr as a chemically active element, Corros. Sci. 52 (2010) 3394–3404.

[32] H. Ali-Löytty, P. Jussila, M. Valden, Optimization of the electrical properties of Ti–Nb stabilized ferritic stainless steel SOFC interconnect alloy upon high-temperature oxidation: The role of excess Nb on the interfacial oxidation at the oxide–metal interface, Int. J. Hydrog. Energy. 38 (2013) 1039–1051.

[33] M. Azizan, T.A.N. Tan, R.C. Cinti, G. Chauvet, R. Baptist, Reactive Nb/Si(111) interfaces studied by electron spectroscopy, Solid State Commun. 54 (1985) 895–898.

[34] L. Vitos, A.V. Ruban, H.L. Skriver, J. Kollár, The surface energy of metals, Surf. Sci. 411 (1998) 186–202.

[35] H. Ali-Löytty, P. Jussila, M. Hirsimäki, M. Valden, Influence of CrN surface compound on the initial stages of high temperature oxidation of ferritic stainless steel, Appl. Surf. Sci. 257 (2011) 7783–7791.

[36] H. Ali-Löytty, P. Jussila, T. Juuti, L.P. Karjalainen, A.A. Zakharov, M. Valden, Influence of precipitation on initial high-temperature oxidation of Ti–Nb stabilized ferritic stainless steel SOFC interconnect alloy, Int. J. Hydrog. Energy. 37 (2012) 14528–14535.

[37] Y. Kato, M. Ito, Y. Kato, O. Furukimi, Effect of Si on Precipitation Behavior of Nb-Laves Phase and Amount of Nb in Solid Solution at Elevated Temperature in High Purity 17%Cr-0.5%Nb Steels, Mater. Trans. 51 (2010) 1531–1535.

[38] M.I. Isik, A. Kostka, V.A. Yardley, K.G. Pradeep, M.J. Duarte, P.P. Choi, D. Raabe, G. Eggeler, The nucleation of Mo-rich Laves phase particles adjacent to M23C6 micrograin boundary carbides in 12% Cr tempered martensite ferritic steels, Acta Mater. 90 (2015) 94–104.

[39] M.I. Isik, A. Kostka, G. Eggeler, On the nucleation of Laves phase particles during high-temperature exposure and creep of tempered martensite ferritic steels, Acta Mater. 81 (2014) 230–240.

[40] P. Jussila, H. Ali-Löytty, K. Lahtonen, M. Hirsimäki, M. Valden, Inhibition of initial surface oxidation by strongly bound hydroxyl species and Cr segregation: H2O and O_2 adsorption on Fe–17Cr, Surf. Sci. 603 (2009) 3005–3010.

[41] J.R. Lince, S.V. Didziulis, D.K. Shuh, T.D. Durbin, J.A. Yarmoff, Interaction of O_2 with the $Fe_{0.84}Cr_{0.16}$(001) surface studied by photoelectron spectroscopy, Surf. Sci. 277 (1992) 43–63.

[42] C.-O.A. Olsson, D. Landolt, Passive films on stainless steels—chemistry, structure and growth, Electrochimica Acta. 48 (2003) 1093–1104.

[43] A. King, G. Johnson, D. Engelberg, W. Ludwig, J. Marrow, Observations of Intergranular Stress Corrosion Cracking in a Grain-Mapped Polycrystal, Science. 321 (2008) 382–385.

[44] S. Swaminathan, C. Mallika, N.G. Krishna, C. Thinaharan, T. Jayakumar, U. Kamachi Mudali, Evolution of surface chemistry and morphology of oxide scale formed during initial stage oxidation of modified 9Cr–1Mo steel, Corros. Sci. 79 (2014) 59–68.

[45] T. Horita, K. Yamaji, H. Yokokawa, A. Toji, T. Uehara, K. Ogasawara, H. Kameda, Y. Matsuzaki, S. Yamashita, Effects of Si and Al concentrations in Fe–Cr alloy on the formation of oxide scales in H_2–H_2O, Int. J. Hydrog. Energy. 33 (2008) 6308–6315.

[46] M.P. Phaniraj, D.-I. Kim, Y.W. Cho, Effect of grain boundary characteristics on the oxidation behavior of ferritic stainless steel, Corros. Sci. 53 (2011) 4124–4130.

[47] Z. Zeng, K. Natesan, Z. Cai, S.B. Darling, The role of metal nanoparticles and nanonetworks in alloy degradation, Nat Mater. 7 (2008) 641–646.

Figure captions:

Fig. 1. (a) SEM image and (b) EBSD inverse pole figure (IPF) coloured map overlaid with band contrast (BC) map of EN 1.4521 sample. (c) EF-PEEM work function map and (d) EF-PEEM image showing relative Cr atomic concentration of the sample after sputter cleaning and annealing at 450 °C for 5 min in UHV. Average Cr concentration on different grains is marked on the figure in (d). The work function and relative Cr concentration were not defined for Ti(CN) and (NbTi)C precipitate areas.

Fig. 2. Normalized XPS intensities of Si 2p, Nb 3d, Ti 2p, Fe 3p, Cr 3p, and Mo 3d during annealing of a sputter cleaned EN 1.4521 sample at 450–800 °C in UHV. The temperature was raised to the target value starting at 450 °C, where XPS spectra were recorded after 5 min stabilization time. After the data acquisition time of 4 min the temperature was increased in 50 °C increments up to 800 °C. The XPS spectra were acquired using the optimal surface sensitivity by selecting an incident photon energy of 400 eV for all transitions except for Ti 2p, where a photon energy of 688 eV was used.

Fig. 3. XP spectra of (a) Si 2p, (b) Nb 3d, and (c) Ti 2p transitions during annealing of an unoxidized EN 1.4521 sample at 25–800 °C in UHV. The temperature was raised to the target value starting at 450 °C, where XPS spectra were recorded after 5 min stabilization time. After the data acquisition time of 4 min the temperature was increased in 50 °C increments up to 800 °C. The XPS spectra were acquired using the optimal surface sensitivity by selecting an incident photon energy of 400 eV for all transitions except for Ti 2p, where a photon energy of 688 eV was used.

Fig. 4. XP spectra of (a) Fe $2p_{3/2}$, (b) Cr $2p_{3/2}$, (c) Mo 3d, (d) Mn 2p, (e) Si 2p, (f) Ti 2p, (g) Nb 3d and (h) O 1s for EN 1.4521 after sputter cleaning and annealing at 450 °C for 5 min (unoxidized), after oxygen exposure in 8.0×10^{-4} Pa O_2 for 2500 s at 25 °C, and after post-annealing at 450, 650, and 800 °C for 30 min in UHV. The spectra were measured using an incident photon energy of 1486.5 eV. Green lines indicate the band pass energy window for EF-PEEM images shown in Figs. 5 and 6.

Fig. 5. EF-PEEM images of Fe 2p, Cr 2p, Mo 3d, Mn 2p and O 1s transitions for EN 1.4521 after sputter cleaning and annealing at 450 °C for 5 min (unoxidized), after oxygen exposure in 8.0×10^{-4} Pa O_2 for 2500 s at 25 °C, and after post-annealing at 450, 650, and 800 °C for 30 min in UHV. Dotted red rectangle indicates location of measured area in Fig. 1. Bright pixels in the EF-PEEM images indicate high atomic concentration. EF-PEEM images of Mn 2p after the O_2 exposure at 25 °C and Mo 3d after post-annealing at 450 °C were not measured.

Fig. 6. EF-PEEM images of Si 2p, Nb 3d and Ti 2p transitions for EN 1.4521 after post-annealing of oxidized sample at 450, 650, and 800 °C for 30 min in UHV. Dotted red rectangle indicates location of measured area in Fig. 1. Bright pixels in the EF-PEEM images indicate high atomic concentration.

Figure 1

Click here to download high resolution image

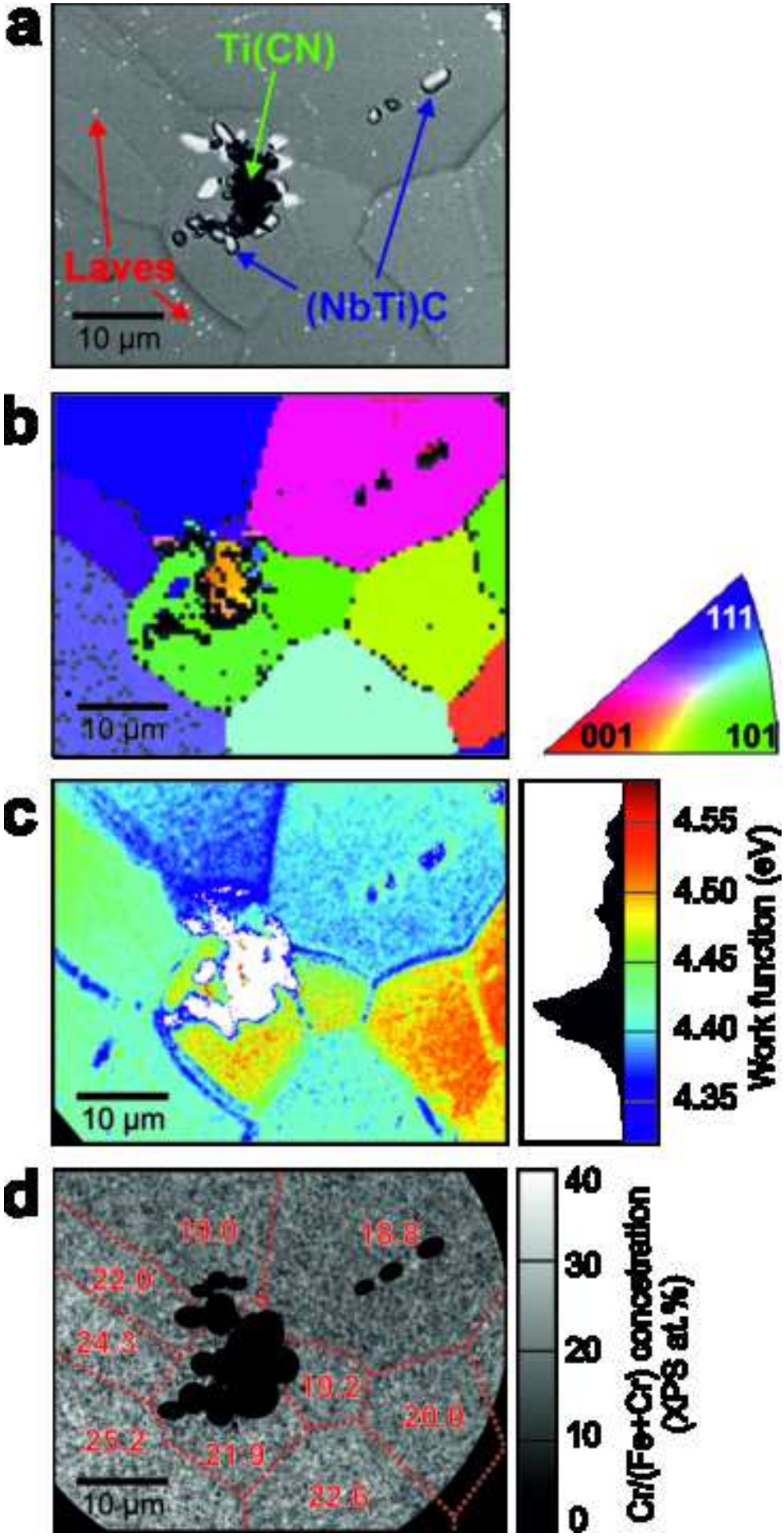

Figure 2

Click here to download high resolution image

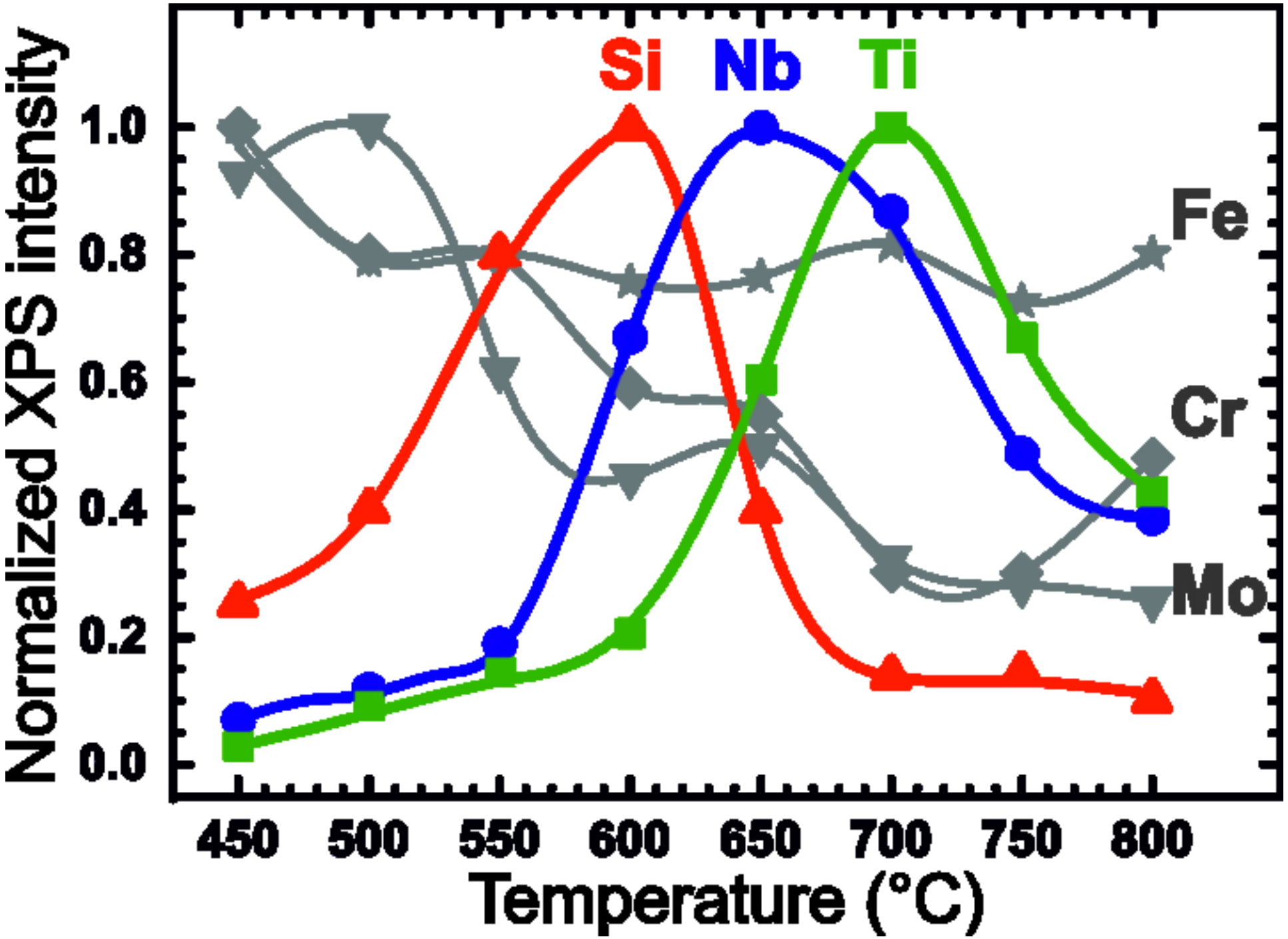

Figure 3

Click here to download high resolution image

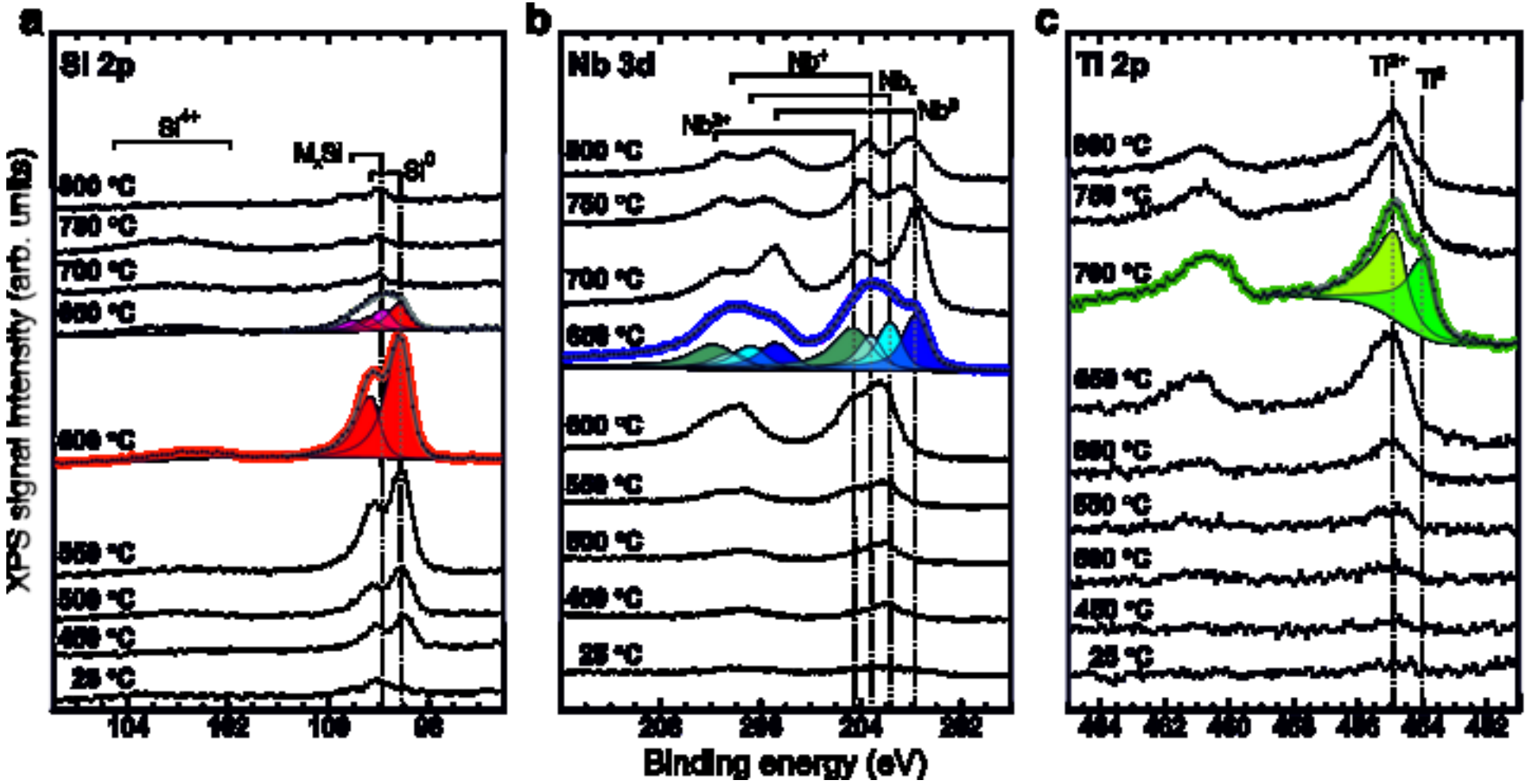

Figure 4

Click here to download high resolution image

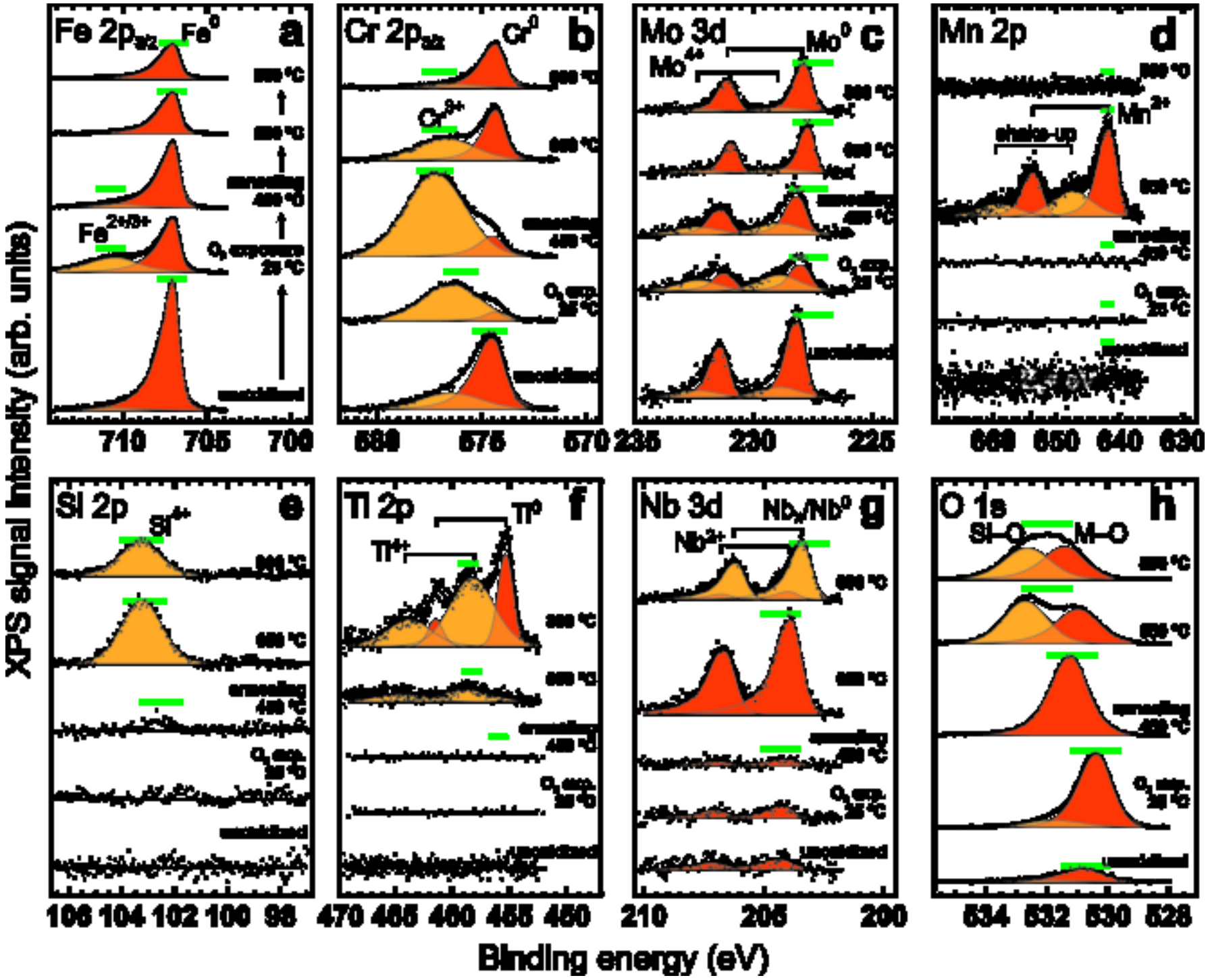

Figure 5

Click here to download high resolution image

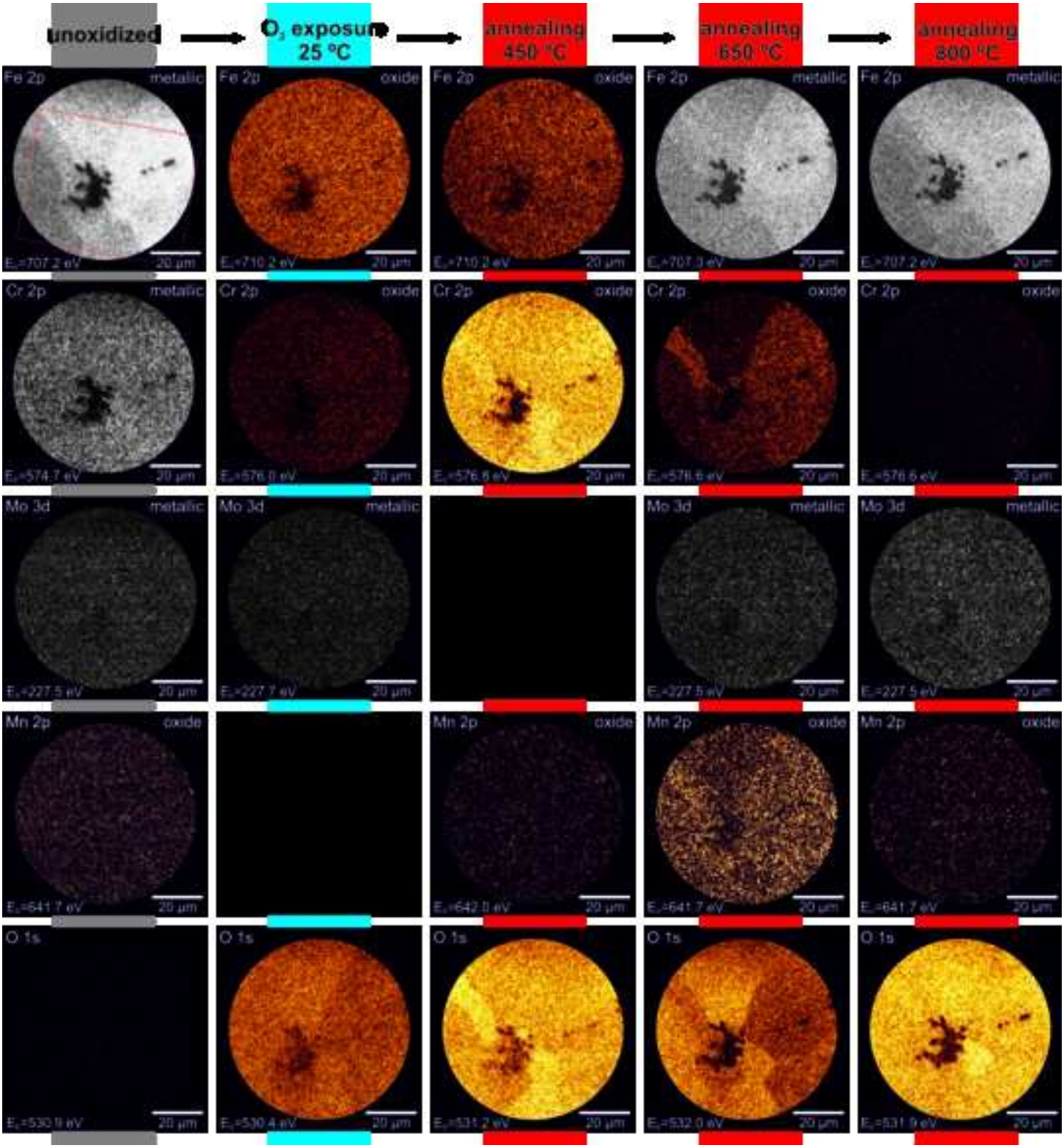

Figure 6

Click here to download high resolution image